Liquid Crystals

ISSN: 0267-8292 (Print) 1366-5855 (Online) Journal homepage: www.tandfonline.com/journals/tlct20

Polarity mapping in liquid crystals using laser-induced heating

Peter Andolšek, Nerea Sebastian, Calum J. Gibb, Jordan Hobbs, Richard J. Mandle, Alenka Mertelj & Natan Osterman

To cite this article: Peter Andolšek, Nerea Sebastian, Calum J. Gibb, Jordan Hobbs, Richard J. Mandle, Alenka Mertelj & Natan Osterman (2025) Polarity mapping in liquid crystals using laser-induced heating, Liquid Crystals, 52:9-10, 792-800, DOI: 10.1080/02678292.2025.2524438

To link to this article: https://doi.org/10.1080/02678292.2025.2524438

LIQUID CRYSTALS
2025, VOL. 52, NOS. 9–10, 792–800
https://doi.org/10.1080/02678292.2025.2524438

Taylor & Francis
Taylor & Francis Group

Polarity mapping in liquid crystals using laser-induced heating

Peter Andolšek[a], Nerea Sebastian[b], Calum J. Gibb[c], Jordan Hobbs[d], Richard J. Mandle[c,d], Alenka Mertelj[b] and Natan Osterman[a,b]

[a]Faculty of Mathematics and Physics, University of Ljubljana, Ljubljana, Slovenia; [b]Complex Matter Department, Jožef Stefan Institute, Ljubljana, Slovenia; [c]School of Chemistry, University of Leeds, Leeds, UK; [d]School of Physics and Astronomy, University of Leeds, Leeds, UK

ABSTRACT

The investigation of phase behaviour in the new class of materials showing ferroelectric nematic and related phases can greatly benefit from methods that combine thermal control with structural and polarity-sensitive imaging. In this work, we present a technique that integrates focused infrared laser heating with second harmonic generation microscopy, enabling rapid, localised control of temperature and simultaneous polarity-resolved imaging. This approach allows for spatially resolved visualisation of multiple coexisting liquid crystalline phases and their polar character in a single-shot experiment – significantly accelerating analysis compared to conventional heating-stage-based methods. We demonstrate the method on conventional nematic LCs and a complex ferroelectric nematic LC, resolving a rich sequence of mesophases and validating induced temperature profiles through numerical simulations. Our approach offers strong potential for high-throughput screening of novel materials and exploration of metastable phases.

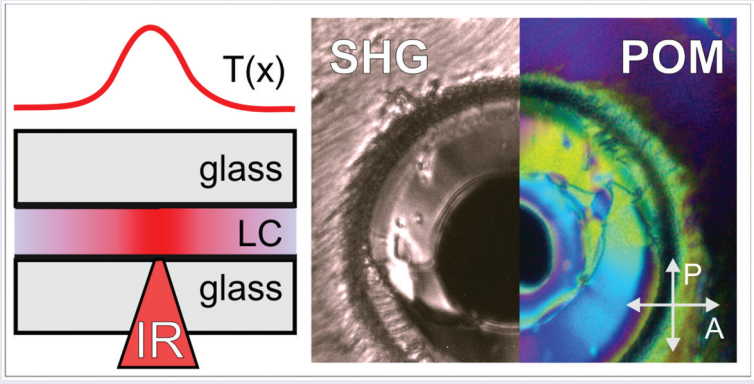

ARTICLE HISTORY
Received 26 May 2025

KEYWORDS
Ferroelectric nematic liquid crystal; laser heating; opto-thermal manipulation; phase coexistence; temperature gradient; SHG microscopy

1. Introduction

Polarising microscopy, often combined with controlled heating stages, is one of the traditional and widely used techniques for studying thermotropic liquid crystals and their phase transitions. To maintain thermal equilibrium across the sample, these systems typically operate at slow temperature ramp rates of around 1 K/min. This careful approach remains crucial for accurately resolving phase structures and ensuring reliable interpretation of phase transitions.

A key challenge when working with ferroelectric liquid crystals is the identification of polar phases, these being a special case of liquid crystals in which the inversion symmetry of the director is broken, giving rise to bulk polarity. The procedure typically begins with a temperature scan to observe the evolution of textures using polarised optical microscopy (POM), followed by differential scanning calorimetry to precisely determine the phase transition temperatures. Finally, second harmonic generation (SHG) microscopy is employed to directly measure the polarity of the mesophases and to extract nonlinear optical coefficients. Although this sequence of measurements provides a thorough and well-established approach to characterising liquid crystalline phases, it involves multiple steps that must be carefully coordinated. There may be some variations between thermal scans due to differences in the calibration of temperature sensors across different devices, which can

CONTACT Natan Osterman natan.osterman@ijs.si
Supplemental data for this article can be accessed online at https://doi.org/10.1080/02678292.2025.2524438

lead to discrepancies in the measured phase transition temperatures and add complexity to the interpretation of mesophase formation.

Moreover, the discovery of novel polar phases and the growing number of synthesised liquid crystal families [1–10], some exhibiting polar phases and some not, call for a more efficient initial screening method. A rapid technique to identify molecules that exhibit polar phases would allow researchers to prioritise those materials for more detailed studies. Although slow cooling and additional experiments will ultimately be necessary to fully characterise the material, this initial rapid screening significantly narrows down the candidates, enabling a more focused investigation of polar materials and phases.

In addition, conventional heating stages are typically limited to temperature ramp rates well below 1 K/s, which makes them less suited for studying dynamic processes or accessing metastable phases that depend on rapid thermal transitions. These constraints underscore the value of alternative methods that offer both precise temperature control and fast thermal modulation.

The development of localised heating techniques, such as the use of a focused infrared (IR) laser, offers a promising alternative by enabling precise, controlled temperature gradients within a sample. This approach creates regions of different temperatures within the same liquid crystal cell, allowing for the local modification of the order parameter or the simultaneous observation of multiple phases under different thermal conditions. In [11], IR light absorption from a tightly focused laser tweezer beam was used to locally heat a thin layer of nematic liquid crystal by several degrees, resulting in a gradient of the order parameter and the transport of particles towards the hot spot. The same group later used stronger IR laser pulses to locally heat the liquid crystal to the isotropic phase and then observed rapid quenching, demonstrating cooling rates of up to 10,000 K/s [12].

The present study employs a focused (or defocused) IR laser to induce localised heating in thermotropic liquid crystal samples with multiple liquid crystalline mesophases, establishing a stable temperature gradient across the sample. This enables real-time phase visualisation and the observation of phase coexistence under varying temperatures. To further enhance the phase analysis, our setup integrates SHG microscopy, a nonlinear optical technique that allows for the direct visualisation of polarity within the liquid crystal phases, providing an additional layer of insight into the structure and behaviour of each phase.

This combined approach of opto-induced heating and SHG microscopy provides a powerful tool for studying liquid crystal phases (Figure 1). By enabling the simultaneous observation of multiple phases within the same sample region and field of view, along with their associated polarity differences, it offers a complementary and efficient alternative to traditional phase characterisation techniques. In this manuscript, we describe the experimental setup, the process of phase observation under controlled temperature gradients, and the insights gained from the simulation of the setup.

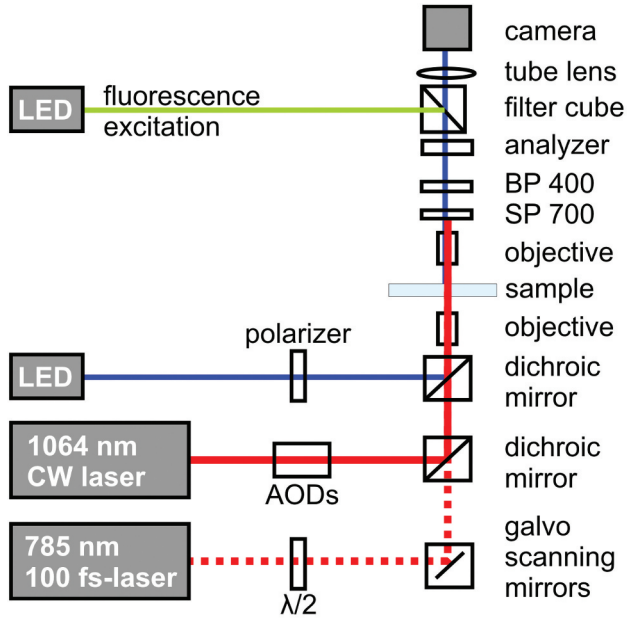

Figure 1. (Colour online) Experimental setup enabling temperature control on a microscale using focused IR heating, along with polarization, fluorescence and SHG imaging.

2. Materials and methods

2.1. Sample preparation

In this study, we used three liquid crystals (LCs): two conventional nematic LCs and one ferroelectric nematic LCs. The two conventional nematics were 5CB (Nematel), a commercially available liquid crystal with the phase sequence Cr – 20.5°C – N – 35.2°C – Iso, and E7 (Merck), a nematic mixture with the phase sequence N – 61°C – Iso. The ferroelectric nematic liquid crystal compound 1 was first reported in [13]; however, we synthesised it following the procedure described in our own work [14]. It exhibits the phase sequence Cr – 67.4°C – SmC_P^H – 90.9°C – N_{TBF} – 103.3°C – N_F – 143.1°C – N_S – 150.7°C – N – 234.1°C – Iso, with all liquid crystalline phases being enantiotropic. It should be noted that the phase transition temperatures differ slightly between [13] and [14]. Similar phase was reported in [15].

Materials were filled at a temperature corresponding to the conventional non-polar nematic phase into glass liquid crystal cells with surfaces imposing in-plane orientation of the director (EHC) of 5 μm and with parallel rubbing. Both top and bottom inside surface of cells were coated with ~ 100 nm thin ITO layer.

2.2. Experimental setup

The experimental setup, shown in Figure 1, integrates precise beam steering, polarisation control, and high-resolution image acquisition for comprehensive optical and thermal analysis.

The samples were observed using bright field and polarised optical microscopy using a LED as a light source. The illumination passed through a rotatable polariser and was then directed along the optical axis of the system using a dichroic mirror. The transmitted light was analysed using a second (rotatable and removable) polariser.

SHG imaging was performed using a custom-built scanning microscope. The laser source is an Erbium-doped fibre laser (C-Fibre A 780, MenloSystems) generating 785 nm, 95 fs pulses at a 100 MHz repetition rate. The average power was adjusted using an ND filter to 10 mW on the sample. A motorised half-waveplate adjusts the incident polarisation on the sample and, jointly with the analyser in front of the camera, enables to perform polarisation-resolved SHG. A combination of galvo mirrors and a long-working distance objective (Nikon CFI T Plan SLWD, NA 0.3, mounted on a piezo stage for a precise displacements along optical axis) is used to scan the focused beam in the sample plane. The scanning frequencies are much higher (a few 100 Hz) than the SHG imaging frame rate (a few Hz).

A long-working distance 20× objective (Nikon CFI T Plan SLWD, NA 0.3) collects the light coming from the sample both for polarised and SHG imaging. A set of 700 nm short-pass and 400 nm band-pass filters eliminates the fundamental IR light and any possible fluorescence signal. The images are finally acquired using a high-performance CMOS camera (Grasshopper 3, Teledyne Flir) with a typical integration time of 250 ms, dimensions 1920 × 1200 pixels, and 0.285 μm/pixel.

Localised sample heating was achieved through the absorption of a focused 1064 nm IR laser beam by the ITO coatings on both substrates of the LC cells. The beam was steered using a pair of acousto-optic deflectors, controlled by a computerised laser tweezers system (Aresis, Tweez 250si). This setup enabled the creation of multiple hot spots through time-sharing of the laser beam, with a switching frequency of up to 100 kHz. The sample is at room temperature before the laser heating is turned on.

The temperature field due to IR absorption was determined in a separate measurement in which an ITO coated cell was filled with BCECF (2',7'-bis-(2-carboxyethyl)-5-(and-6)-carboxyfluorescein) dissolved in a 1 mM TRIS buffer solution. BCECF exhibits temperature-dependent fluorescence intensity, allowing for precise thermal mapping. Upon excitation with a suitable light source, the fluorescence emission of BCECF decreases with increasing temperature due to changes in its quantum yield. By calibrating the fluorescence intensity against known temperature values in a heating stage (Instec HCS412W), a reliable relationship between fluorescence and temperature was established, $T = T_0 - T^* \ln(I/I_0)$ where I_0 is the fluorescence intensity at ambient temperature T_0 and I the measured intensity at an increased temperature T. This calibration enabled the measurement of spatial temperature variations in the sample calculated from the fluorescence image of the BCECF dye taken immediately after the laser heating was turned on in order to avoid thermophoretic depletion and thus incorrect temperature determination.

3. Results

3.1. Uniform heating of large regions

We first attempted to create regions of uniform temperature. Figure 2(a) shows the measured temperature field of a 90 μm × 60 μm rectangular region, generated by time-sharing the heating laser beam. A homogeneous temperature increase was achieved by sequentially focusing the laser onto a grid of $N = 30 \times 20$ equally spaced points. The laser remained at each point for 10 μs ($f = 100$ kHz) before randomly moving to another point in the grid, repeating the process continuously. The random ordering of the heating points was necessary to prevent fluid flows caused by the thermo-viscous pumping effect [16,17].

The resulting temperature profiles along the x-axis for different laser powers are shown in Figure 2(b). With increasing laser power, both the peak temperature and the temperature in the surrounding area rise. The peak temperature is linearly proportional to the laser power, as demonstrated in Figure 2(c).

When 5CB was exposed to homogeneous heating conditions (Figure 2(d), Video 1 in SI), we immediately observed 'flickering' within the heated region, indicating that the temperature was far from uniform. This effect arises due to the time-sharing operation of the heating laser. During time-sharing,

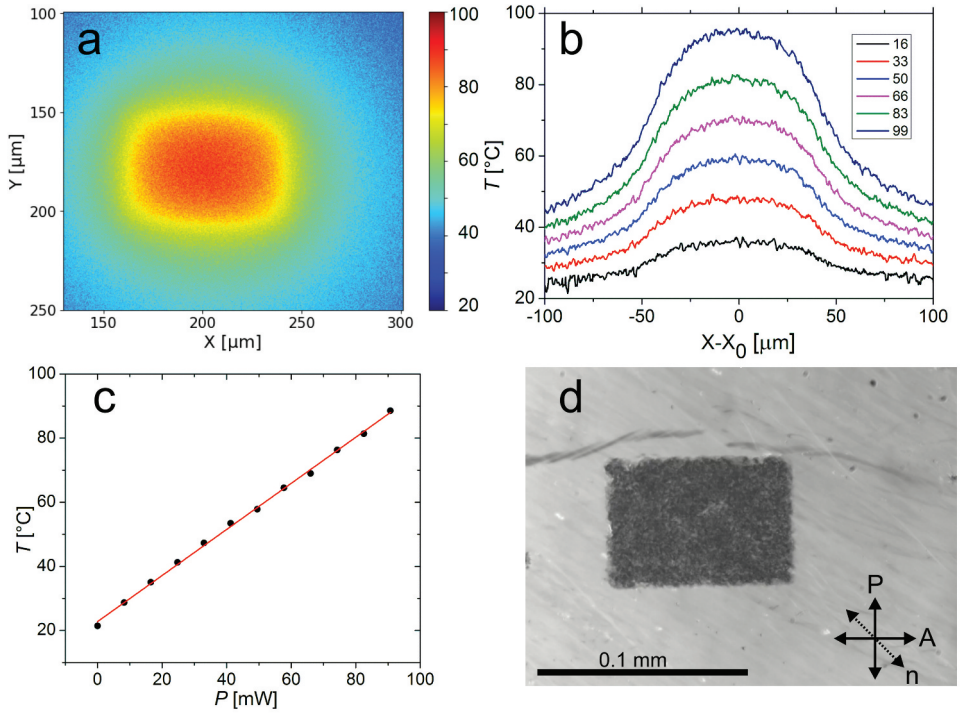

Figure 2. (Colour online)Homogeneous heating, achieved through time-shared illumination of a rectangular region measuring 90 µm × 60 µm, consisting of 600 equally spaced heating points. a) The resulting temperature field, obtained using temperature-dependent fluorescence. The color bar indicates the temperature in °C. b) Temperature profile across the horizontal axis. Different colors represent various heating laser powers, given in mW. c) Maximum temperature increase as a function of laser power. d) Grainy, non-stationary 5CB structure exhibiting rapid temporal evolution. Arrows indicate the directions of the polarizer (P), analyzer (A), and the rubbing direction (n).

the laser locally heats a small region around its current focal point, causing the liquid crystal to transition into the isotropic phase. The laser then sequentially moves to $N-1$ other points before returning to the starting position. The complete cycle takes $t = \frac{N}{f} = 6\,\text{ms}$.

A rough estimate of the characteristic cooling time is given by

$$\tau = \frac{a^2 \rho c_p}{k},$$

where cooling predominantly occurs through the upper and lower glass plates. For a typical sample size of $a = 10$, with the glass having a density (ρ) of 2230 kg/m^3, a specific heat capacity (c_p) of 830 J/(kgK), and a thermal conductivity (k) of 1.1 W/(mK), we obtain a cooling time of $\tau \approx 0.16$ms.

Since the cooling time is significantly shorter than the laser round-trip time, the LC transitions back from the isotropic to the nematic phase before the laser returns. As this process occurs at every point of the heating grid, it results in the observed flickering effect. Heating large areas using a time-shared focused laser beam is therefore unsuitable for typical LC cells.

3.2. Single point heating

Instead of large-area heating using multiple points, we next investigated static single-point heating with a focused laser. The resulting temperature profiles along the x-axis for two different laser powers are presented in Figure 3(a). The full width at half maximum (FWHM) of the temperature profile is less than 30 µm, while the thermal gradient reaches values as high as 7 K/µm. Both the FWHM and the maximum achievable gradient are strongly influenced by the thickness of the LC layer and the beam waist of the heating laser. These dependencies are examined in detail below in the Simulation section.

To reduce temperature gradients, we systematically shifted the focus of the heating laser by a fixed amount along the optical axis. This deliberate defocusing resulted in an expanded FWHM of the temperature distribution, leading to a more gradual thermal gradient. The broader heated region allowed for the simultaneous observation

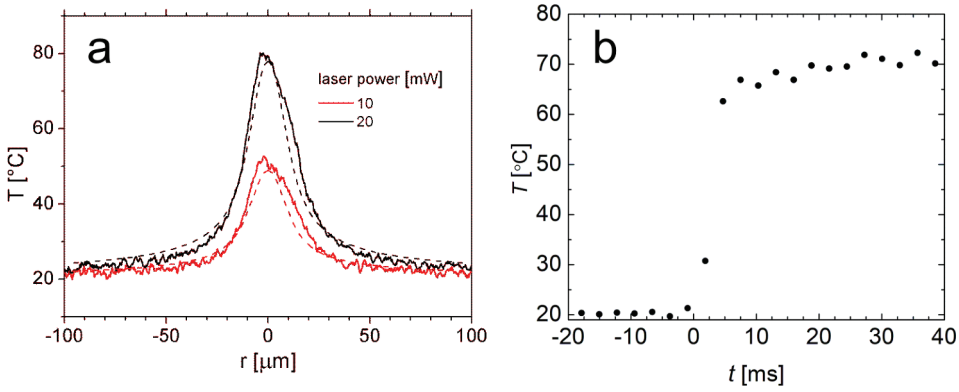

Figure 3. (Colour online) Single-point heating. (a) Temperature profiles for two different laser powers. Solid lines represent the measured data, while dashed lines indicate the simulation results. (b) Temporal evolution of the maximum sample temperature. The heating laser is switched on at $t = 0$.

of multiple LC phases emerging between the isotropic state and room temperature. This approach provides a controlled thermal environment for studying phase transitions with enhanced spatial resolution.

In Figure 3(b), we show the measured peak temperature during the switching on of the heating laser. Since the temperature field is determined from fluorescence measurements, the minimum duration of a single measurement is limited by the fluorescence intensity. To achieve an adequate signal-to-noise ratio, the camera acquisition rate was set to 300 Hz. The camera was not externally synchronised with the laser control, so we defined $t = 0$ as the last data point having room temperature. It can be seen that the temperature jump occurs within one or two frames, i.e. in less than 6 ms.

3.3. Simulation

We numerically solved the heat equation to obtain temperature field using a finite element solver (Comsol, FEMLAB). Since the problem in the case of focused or defocused point heating is axially-symmetric with the respect to the optical axis, only 2D simulation of the experimental chamber had to be performed.

The geometry along the optical axis (z-direction) was the following: 700 µm thick borosilicate glass, d =100 nm thick ITO layer, 5 µm of liquid crystal, covered by 100 nm of ITO and 700 µm glass. The size of simulated region in the transverse direction (r-direction) was 5000 µm. The laser-induced heating was simulated by a homogeneous absorption of a Gaussian laser beam in ITO layers. We neglected the absorption in the LC layer.

The intensity of the beam is $I(r) = \frac{2P_0}{\pi w_0^2}\exp(-\frac{2r^2}{w_0^2})$, where P_0 is the laser power at the sample position, and w_0 beam waist size at the position of ITO layer. The absorbed power in the first ITO layer is approximately $P_{\mathrm{abs}} = \alpha d P_0$ with α = 11503/cm being the absorption coefficient of ITO on glass at the laser wavelength [18]. The source term, needed to numerically solve the heat equation, is the absorbed power density $P_{abs}/V = \alpha d P_0/(Sd) = \alpha I(r)$. The second ITO layer is hit with a decreased laser power due to the absorption of the first layer therefore the absorbed power density is $P_{abs}/V(1-\alpha z)$.

The heat transfer from the LC cell to the surrounding ambient air was simulated by setting the the heat transfer coefficient at the outside boundaries of the glass plates to $h = 25\frac{W}{m^2\mathrm{K}}$.

Simulated temperature profiles in the middle of LC layer are presented in Figures 3 and 4. At a given heating laser power, the profile strongly depends on the beam waist size w_0 as demonstrated in Figure 4(a). A slight defocusing of the beam dramatically changes the peak temperature. In the experiment we therefore always first focused the beam to reach the highest peak temperature and then used piezo stage to defocus the beam to reach desired beam waist. In Figure 3(a) we compare the experimentally determined temperature profiles with the simulation results for $w_0 = 16$µm. The simulation shows a good agreement with the experimental data, capturing the key trends and exhibit reasonable accuracy.

Simulation can also provide insight into the detailed dynamics of the heating. In Figure 3(b), we show temperature profiles at different times after the heating laser is switched on. As already estimated in Subsection 3.1, it takes on the order of 10^{-4} s for a significant change of LC temperature to occur in this geometry. In the context of time-shared heating using multiple laser points with a switching

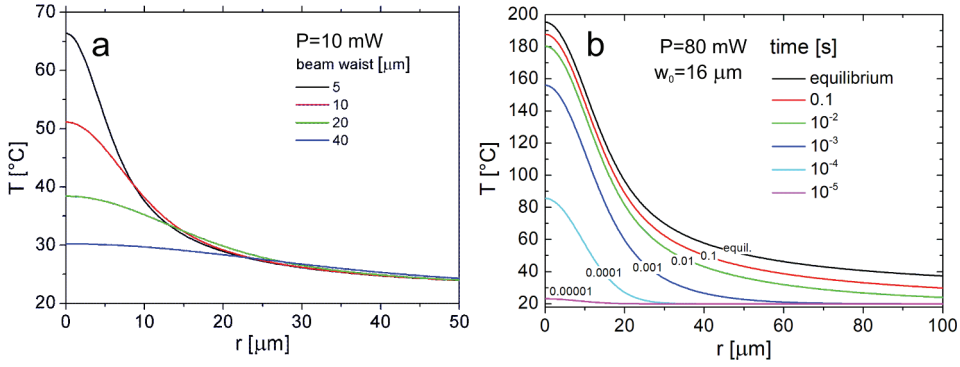

Figure 4. (Colour online) Simulation results. (a) Equilibrium temperature profiles for various beam waists w_0 at a fixed laser power of $P = 10$ mW. (b) Temperature profiles at different times after the heating laser is switched on. The simulation parameters are $P = 80$ mW and $w_0 = 16$ µm.

frequency $f = 100$ kHz, this implies that only a few heating points can be used; otherwise, the local temperature changes significantly during the roundtrip time. This can result in rapid phase transitions, as indicated by the flickering of LC in Supplemental Video 1.

3.4. Nematic liquid crystals

Having characterised and simulated the system, we now apply focused laser heating to generate controlled thermal gradients in real liquid crystals. As a demonstration, we use two well-known nematic materials: 5CB and E7. These classic systems allow us to explore the thermal response and phase behaviour under localised heating, showcasing the potential of our approach for studying temperature-dependent phenomena in liquid crystals with high spatial precision.

In Figure 5 we show POM images of 5CB and E7, which, under given conditions, exhibit only two phases, nematic and isotropic, with the latter appearing dark under crossed polarisers. The appearance of the nematic phase depends on the order parameter which is reduced close to the nematic-isotropic border [11]. One can observe how the size of the isotropic region in 5CB expands with increased laser power. When comparing 5CB and E7 heated with the same power, the isotropic region of E7 is significantly smaller due to its higher transition temperature.

3.5. Ferroelectric liquid crystal

As an exemplar, we present LC compound 1, which exhibits two non-polar and three polar mesophases. Our experimental setup allows us to distinguish between them in a single-shot experiment.

Figure 6 illustrates the rich mesophase sequence of compound 1, observed using two complementary approaches. The composite image consists of simultaneously captured SHG and polarised optical microscopy (POM) image. This configuration enables spatial

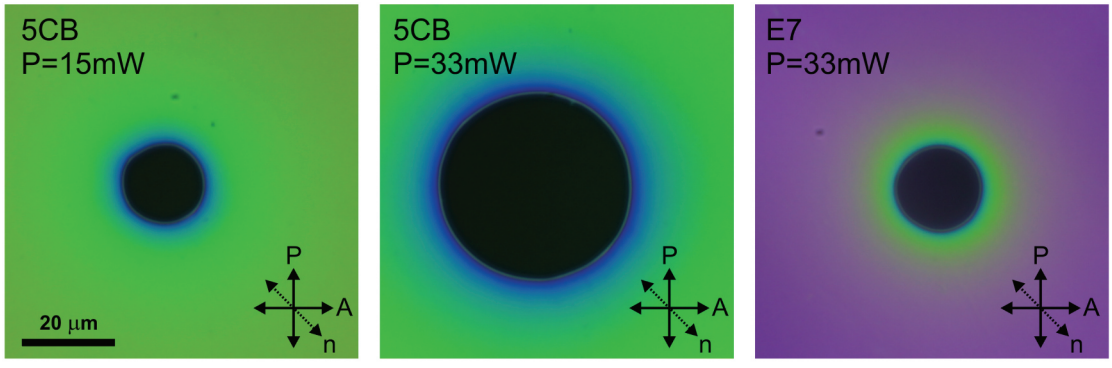

Figure 5. (Colour online) Point heating of 5CB and E7 using different laser powers, as seen under crossed-polarisers. Arrows indicate the directions of the polariser (P), analyser (A), and the rubbing direction (n).

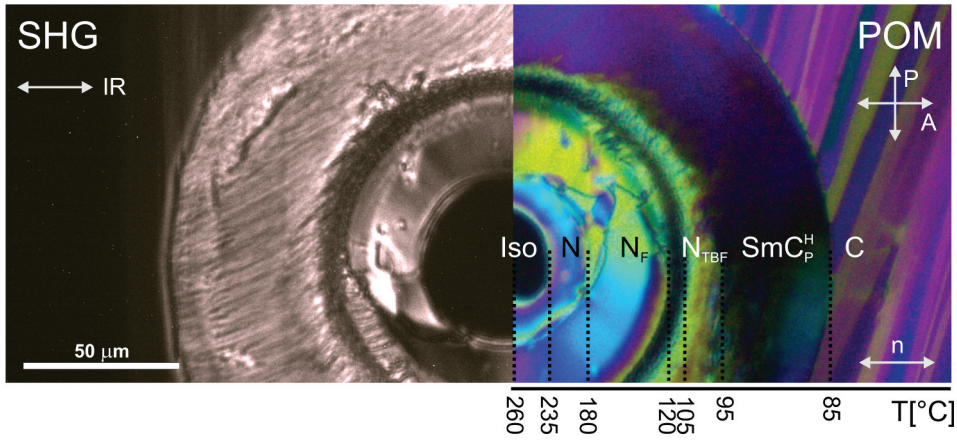

Figure 6. Mesophases of compound 1 resulting from point heating, observed using SHG imaging (left) and polarized optical microscopy (right). Starting from the central isotropic region, four additional phases are visible before reaching the outer crystalline phase. The axis below indicates the temperatures at the marked points. The arrow in the SHG image indicates the direction of the incoming fundamental 785 nm beam used for SHG imaging. The arrows in the POM image indicate the directions of the polarizer (P), analyzer (A), and the rubbing direction (n).

resolution of multiple mesophases coexisting in a radial thermal gradient. Starting from the central isotropic region, four mesophases emerge before the outer crystalline phase is reached. First, a nematic phase appears, characterised by the absence of SHG signal, indicating non-polar order. The boundary with the next phase is not clearly defined, and the N_S phase, expected in this region, could not be reliably identified, likely due to the narrow temperature window of 7 K and steep thermal gradient. Following this, a nematic texture with evident SHG activity emerges, corresponding to the polar N_F phase. This is succeeded by a grainier texture typical of the N_{TBF} phase. As the temperature decreases further, the SmC_P^H phase develops, distinguished by strong SHG activity. Finally, the system transitions into the crystalline phase, which interestingly still exhibits some residual, low-level SHG signal.

The axis at the bottom of Figure 6 presents the temperatures at the detected phase boundaries, obtained from the measured temperature profile for such heating conditions. Although the thermal gradient introduces some spatial averaging and uncertainties due to the finite resolution of the optical system and the steepness of the gradient, a conservative estimate suggests that the transition temperatures can be determined with an accuracy of approximately 10 K. This level of precision is sufficient for rapid phase screening and initial material characterisation.

To further characterise the polar properties of the observed mesophases, we performed a polarisation-

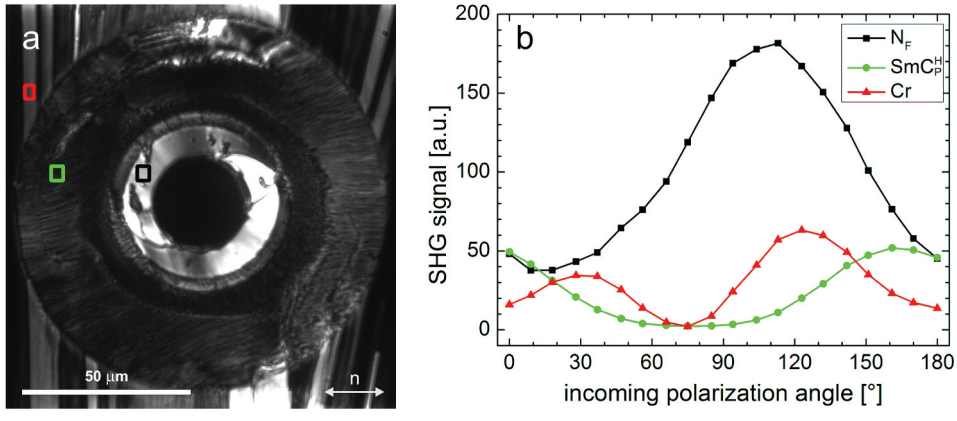

Figure 7. (Colour online) Simultaneous SHG analysis of different phases of compound 1. a) SHG image. b) SHG signal as a function of the polarization angle of the incoming fundamental 785 nm beam. The data is presented for the regions highlighted in (a), each corresponding to a different LC phase. The polarization angle of the fundamental beam in (a) is 123° and the arrow (n) indicates the rubbing direction.

resolved SHG analysis, presented in Figure 7. The angular dependence of the SHG intensity reveals the degree of molecular alignment, the presence of polar domains, and the symmetry of each phase. Strong anisotropy indicates well-aligned polar order, while weak or isotropic responses suggest disordered or multidomain structures.

The orientation of the mesophases arises from a combination of surface anchoring – imposed by the rubbing direction – and the radial temperature gradient induced by localised laser heating. This interplay shapes the polarisation dependence of the SHG signal, particularly near phase boundaries where elastic and thermal effects are pronounced. In the region outside the heated area, the rubbing direction appears to play a negligible role. Instead, the observed stripe patterns align with the direction of the moving SmC_P^H-crystalline phase boundary during cooling. This moving boundary originates from the initial filling of the cell in the isotropic phase; as the sample cools, successive phase transitions occur with phase boundaries sweeping across the cell. The final travelling boundary, corresponding to the SmC_P^H–Cr transition, ultimately dictates the orientation of the resulting crystal domains.

4. Conclusions and outlook

We demonstrated a powerful approach for rapid material screening and polarity mapping in liquid crystals by combining localised infrared laser heating with second harmonic generation microscopy. This method enables the creation of steep, spatially controlled temperature gradients within a single LC sample, allowing for the simultaneous observation of multiple coexisting mesophases. While conventional heating stages offer reliable thermal control and are widely used for phase characterisation, they are inherently optimised for equilibrium studies and sequential measurements. In contrast, our approach enables rapid and concurrent assessment of optical texture and polarity, offering a substantial reduction in experimental time. However, this gain in speed comes at the cost of reduced precision in determining exact phase transition temperatures and requires relatively sophisticated and costly instrumentation. Simulations confirm that the thermal gradients generated by focused laser heating can be finely tuned through beam parameter adjustment, and our experiments validate the effectiveness of this method for both conventional and ferroelectric nematic liquid crystals.

We applied this method to well-known nematic LCs (5CB and E7) as well as to the complex ferroelectric LC compound 1, successfully resolving several mesophases and their polarity states in a single-shot experiment. The spatial overlap of these phases within a stable gradient field provided a unique opportunity for direct comparison, while the SHG analysis revealed polar and non-polar character with high sensitivity. In future studies, by implementing interferometric SHG techniques [19,20], it would be possible not only to detect the presence of polarity but also to resolve the polarity direction within each mesophase, offering a more detailed and quantitative understanding of the polar structure and its evolution across phase boundaries.

Additionally, our system offers a unique capability for inducing rapid, localised temperature changes – at speeds unattainable with conventional heating stages typically used in liquid crystal research. Such rapid changes could potentially access previously unreachable phases, providing new avenues for exploring phase behaviour and transitions. This is particularly relevant for systems in which polar phases are monotropic and highly unstable [21]; in such cases, the ability to trigger and observe these transient states before they decay or transform is crucial, and our approach provides a practical means of capturing them in situ.

Author contributions

P.A. performed experiments. N.S. prepared the LC cells and together with A.M. assisted in the interpretation of experiments. C.J.G, J.H. and R.J.M. synthesised and characterised compound 1. N.O. designed and coordinated the work and wrote the initial draft of the paper, and all the authors made contributions to the final version.

Acknowledgments

This work was financially supported by the Slovenian Research and Innovation Agency (grants J2–50089 and P1–0192). R.J.M. thanks UKRI for funding via a Future Leaders Fellowship, grant number MR/W006391/1. N. O. used ChatGPT (OpenAI, May 2024) to improve the English language of the manuscript.

Disclosure statement

No potential conflict of interest was reported by the author(s).

ORCID

Nerea Sebastian http://orcid.org/0000-0002-9156-1895
Alenka Mertelj http://orcid.org/0000-0002-2766-9121

References

[1] Mandle RJ, Cowling SJ, Goodby JW. Rational design of rod-like liquid crystals exhibiting two nematic phases.

Chem Eur J. 2017;23(58):14554–14562. doi: 10.1002/chem.201702742
[2] Mandle RJ, Cowling SJ, Goodby JW. A nematic to nematic transformation exhibited by a rod-like liquid crystal. Phys Chem Chem Phys. 2017 May;19(18):11429–11435. doi: 10.1039/C7CP00456G
[3] Nishikawa H, Shiroshita K, Higuchi H, et al. A fluid liquid-crystal material with highly polar order. Adv Mater. 2017;29(43):1702354. doi: 10.1002/adma.201702354
[4] Li J, Xia R, Xu H, et al. How far can we push the rigid Oligomers/Polymers toward ferroelectric nematic liquid crystals?. J Am Chem Soc. 2021 Oct;143(42):17857–17861. doi: 10.1021/jacs.1c09594
[5] Manabe A, Bremer M, Kraska M. Ferroelectric nematic phase at and below room temperature. Liq Cryst. 2021 Jun;48(8):1079–1086. doi: 10.1080/02678292.2021.1921867
[6] Cruickshank E, Pearson A, Brown S, et al. The ferroelectric nematic phase: on the role of lateral alkyloxy chains. Liq Cryst. 2023 Sep;50(11–12):1960–1967. doi: 10.1080/02678292.2023.2221651
[7] Nishikawa H, Kuwayama M, Nihonyanagi A, et al. Rapid, solvent-minimized and sustainable access to various types of ferroelectric-fluid molecules by harnessing mechano-chemical technology. J Mater Chem C. 2023;11(37):12525–12542. doi: 10.1039/D3TC02212A
[8] Tufaha N, Cruickshank E, Pociecha D, et al. Molecular shape, electronic factors, and the ferroelectric nematic phase: investigating the impact of structural modifications. Chem Eur J. 2023 May;29(28):e202300073. doi: 10.1002/chem.202300073
[9] Li J, Wang Z, Deng M, et al. General phase-structure relationship in polar rod-shaped liquid crystals: importance of shape anisotropy and dipolar strength. Giant. 2022 Aug;11:100109. doi: 10.1016/j.giant.2022.100109
[10] Gibb CJ, Hobbs J, Mandle RJ. Systematic fluorination is a powerful design strategy toward fluid molecular ferroelectrics. J Am Chem Soc. 2025 Feb;147(5):4571–4577. doi: 10.1021/jacs.4c16555
[11] Škarabot M, Lokar Ž, Muševič I. Transport of particles by a thermally induced gradient of the order parameter in nematic liquid crystals. Phys Rev E. 2013 Jun;87(6):062501. doi: 10.1103/PhysRevE.87.062501
[12] Jagodič U, Ryzhkova A, Muševič I. Localised opto-thermal response of nematic liquid crystal to laser light. Liq Cryst. 2019 May;46(7):1117–1126. doi: 10.1080/02678292.2018.1557270
[13] Karcz J, Herman J, Rych-Lowicz N, et al. Spontaneous chiral symmetry breaking in polar fluid–heliconical ferroelectric nematic phase. Science. 2024 Jun;384(6700):1096–1099. doi: 10.1126/science.adn6812
[14] Hobbs J, Gibb CJ, Mandle RJ. Ferri- and ferro-electric switching in spontaneously chiral polar liquid crystals. arxiv Prepr. 2025;ArXiv:2502.08551.
[15] Nishikawa H, Okada D, Kwaria D, et al. Emergent ferroelectric nematic and heliconical ferroelectric nematic states in an achiral “straight” polar Rod Mesogen. Adv Sci. 2024 Oct;11(39):2405718. doi: 10.1002/advs.202405718
[16] Weinert FM, Kraus JA, Franosch T, et al. Microscale fluid flow induced by thermoviscous expansion along a traveling wave. Phys Rev Lett. 2008 Apr;100(16):164501. doi: 10.1103/PhysRevLett.100.164501
[17] Škarabot M, Osterman N, Muševič I. Optothermally driven colloidal transport in a confined nematic liquid crystal. Soft Matter. 2017;13(13):2448–2452. doi: 10.1039/C7SM00136C
[18] Minenkov A, Hollweger S, Duchoslav J, et al. Monitoring the electrochemical failure of indium tin oxide electrodes via operando ellipsometry complemented by electron microscopy and spectroscopy. ACS Appl Mater Interfaces. 2024 Feb;16(7):9517–9531. doi: 10.1021/acsami.3c17923
[19] Yazdanfar S, Laiho LH, So PTC. Interferometric second harmonic generation microscopy. Opt Express. 2004 Jun;12(12):2739–2745. doi: 10.1364/OPEX.12.002739
[20] Sebastián N, Lovšin M, Berteloot B, et al. Polarization patterning in ferroelectric nematic liquids via flexoelectric coupling. Nat Commun. 2023 May;14(1):3029. doi: 10.1038/s41467-023-38749-2
[21] Li J, Nishikawa H, Kougo J, et al. Development of ferroelectric nematic fluids with giant-ε dielectricity and nonlinear optical properties. Sci Adv. 2021 Apr;7(17):eabf5047. doi: 10.1126/sciadv.abf5047